Optical and microstructural properties of electrodeposited cuprous oxide

Stanislav Jurečka[1] · Prangya P. Sahoo[1] · Peter Čendula[1]

Abstract

The production of hydrogen fuel using photoelectrochemical water splitting method requires semiconductor materials with suitable energy gap, electrical and optical properties. Cuprous oxide is feasible candidate fulfilling many of these requirements to be the photocathode of such devices. In this study, we investigated optical and microstructural properties of cuprous oxide prepared under different temperatures. Microstructure properties were evaluated by statistical, fractal and Fourier methods. Roughness characteristics, Fourier transforms and multifractal characteristics provide consistent information connected with the distribution of surface objects created during sample fabrication. Our methodology is feasible to provide practical insights for the fabrication and monitoring of surface and optical properties of Cu_2O and other semiconductor materials.

Keywords Hydrogen · Water splitting · Cu_2O · AFM · Raman scattering · Microstructure analysis

1 Introduction

To balance the increasing energy consumption, it is important to exploit renewable energy sources. In the recent past, a lot of research effort was made to produce renewable hydrogen fuel. One of the large variety of approaches for renewable hydrogen production is based on the photoelectrochemical water splitting (PEC). Photocatalytic decomposition of water into hydrogen and oxygen using semiconductors and solar energy has a great economic and environmental potential. The scientific and engineering challenges that must be addressed to make this technology economical were recently discussed [1].

One of the promising semiconductor materials for generation of hydrogen from water splitting under visible light irradiation is cuprous oxide (Cu_2O). Among the various metal oxide materials, Cu_2O has a suitable band gap, high absorption coefficient in the visible-light region, good optical and electrical properties. It is made of earth abundant elements, non-toxic and low-priced [2]. Cu_2O is used in applications such as gas sensing [3], solar cells [4, 5], photocatalysis [6], and photoelectrodes for solar water splitting [7–9]. Various

synthesis methods are used to prepare Cu_2O thin films such as pulsed laser deposition [10], chemical vapor deposition [11] and electrodeposition [12–16]. The electrodeposition method provides several advantages because of its simplicity, low cost, and the possibility of forming large area samples. It allows the control over the stoichiometry, grain size, crystallinity, morphology, and thickness of formed layers. Cu_2O films are usually electrodeposited from a copper precursor solution, such as copper nitrate, copper acetate or copper sulfate.

In the current study, we have prepared Cu_2O thin films on conductive glass substrates by the electrodeposition technique in a solution containing copper sulfate with lactic acid at different temperatures. The effect of deposition temperature on formed layers was studied by optical methods (Raman scattering and UV–Vis spectroscopy) and properties of the resulting surface microstructure was investigated by the atomic-force microscopy (AFM) and analyzed by the latest statistical, fractal and Fourier methods.

2 Experiment

The Cu_2O layers were prepared from an aqueous solution of copper sulfate and lactic acid [17] on fluorine-doped tin oxide (FTO) glass slides. The FTO glass slides were cleaned by sonication in deionized water followed by ethanol and

✉ Peter Čendula
  peter.cendula@feit.uniza.sk

1 Institute of Aurel Stodola, University of Žilina, Komenskeho 843, 03101 Liptovský Mikuláš, Slovakia

acetone for thirty minutes each to remove the impurities. The pH of the forming solution was set to 12 by adding 3 M NaOH. Thin films were prepared on FTO coated glass substrates by a potentiostatic electrodeposition method for 1 h. A fixed potential of -0.5 V vs. Ag/AgCl reference electrode was applied to the substrates using of a potentiostat–galvanostat Biologic SP-150. Samples were prepared at different temperatures: sample A at 25 °C and sample B at 50 °C. After the electrodeposition, the films were rinsed with deionized water and dried in air.

Raman spectra of the thin films were collected by Thermo Scientific DXR Raman spectrometer with 532 nm laser wavelength and analyzed by Avasoft8 software package. UV–Vis spectral reflectance was determined by Avantes 2048 spectrophotometer.

The surface morphology of formed samples was experimentally examined by atomic force microscopy (AFM) using the AIST-NT Smart SPM system. AIST-NT cantilevers produced by AIST Nano Technologies BV, Apeldoom, the Netherlands, were used. Tip height was 10 μm, tip cone angle 22°, and tip curvature radius 10 nm. Four rectangular areas were selected on the samples in order to assess the uniformity of the spatial distribution of the observed geometric objects at the surface of the sample. A set of four samples was analyzed and in all cases the distribution of surface objects was without significant changes. The AFM figures present the results obtained from AFM scans from the middle part of the formed samples. We employed the semi-contact AFM mode, in which the interaction of the cantilever with the investigated surface objects is evaluated based on the change in the oscillations of the cantilever in a defined position above the surface area. In this way, the entire selected surface area is examined. Before the actual measurement, we carefully set all the parameters for the implementation of the semi-contact method in order to achieve a contrast image without damaging the cantilever or the sample. The disadvantage of such a procedure is the construction of a convolution model of the oscillating tip with the investigated surface due to the dynamics of the cantilever vibrations above the surface. Hence we remark this can introduce artifacts in AFM images as a consequence of an imperfect mathematical model of convolution of the tip.

3 Results and discussion

The crystalline phases in the formed cuprous oxide layers were determined by Raman spectroscopy. In our work, Raman spectrum was recorded in the range of 50–1300 cm^{-1}. The phases of Cu and Cu_2O possess highly symmetric cubic structure and CuO is a low symmetry monoclinic structure. The copper oxide particles provide response in the Raman spectrum. The group theory shows that Raman activity is a function of the space group symmetry. The monoclinic CuO structure provides three Raman active optical-phonon modes at 303, 350 and 636 cm^{-1}. Experimentally observed frequencies around 220, 410 and 630 cm^{-1} of the samples A and B correspond to Cu_2O active Raman modes, [18] see Fig. 1, because the modes 303, 350 cm^{-1} typical for CuO are absent.

The properties of the surface microstructures were experimentally studied by the AFM microscopy, Fig. 2. We represented the AFM values by a random height function $h(x,y)$ describing the height of the point above the reference plane at the (x,y) position [19]. We transformed values in the $h(x,y)$ matrix by the 2D Fourier transformation and analysed the structure of the Fourier domain. Values in the Fourier domain coded into the colour scale are shown in Fig. 2. With the increased deposition temperature, the large central part of the 2D Fast Fourier Transform (FFT) image indicates size of the surface features. It is caused by the changes of space frequencies in the formed structures caused by the different temperature conditions during the deposition. The analysis of Fourier domain structure of the $h(x,y)$ function can be, therefore, used for the optimization of the deposition technique.

The properties of the random height function $h(x,y)$ values were examined by statistical methods. R_{RMS} is the root mean square of the $h(x,y)$ values measured from the mean value and Ra is the arithmetic average of the absolute values of the $h(x,y)$ deviations. We also determined other important surface roughness characteristics, higher moments of the $h(x,y)$ function—skewness Rsk and kurtosis Rku [20]. The resulting statistical characteristics of the surface roughness are shown in Table 1.

Both R_{RMS} and Ra values increase with the forming temperature and the deviations are emphasized. The computation of the skewness value Rsk is based on the third
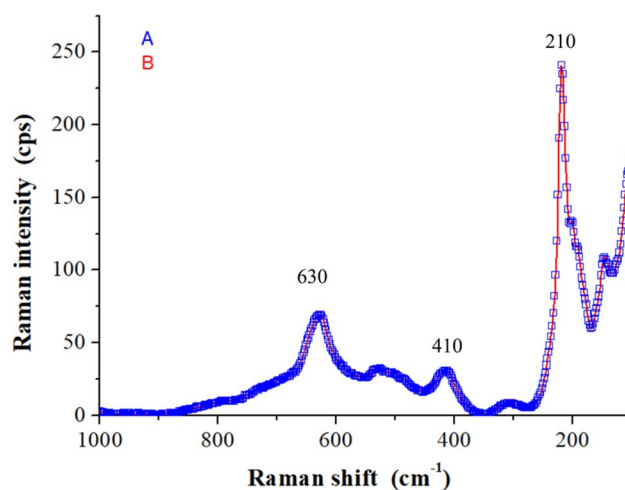

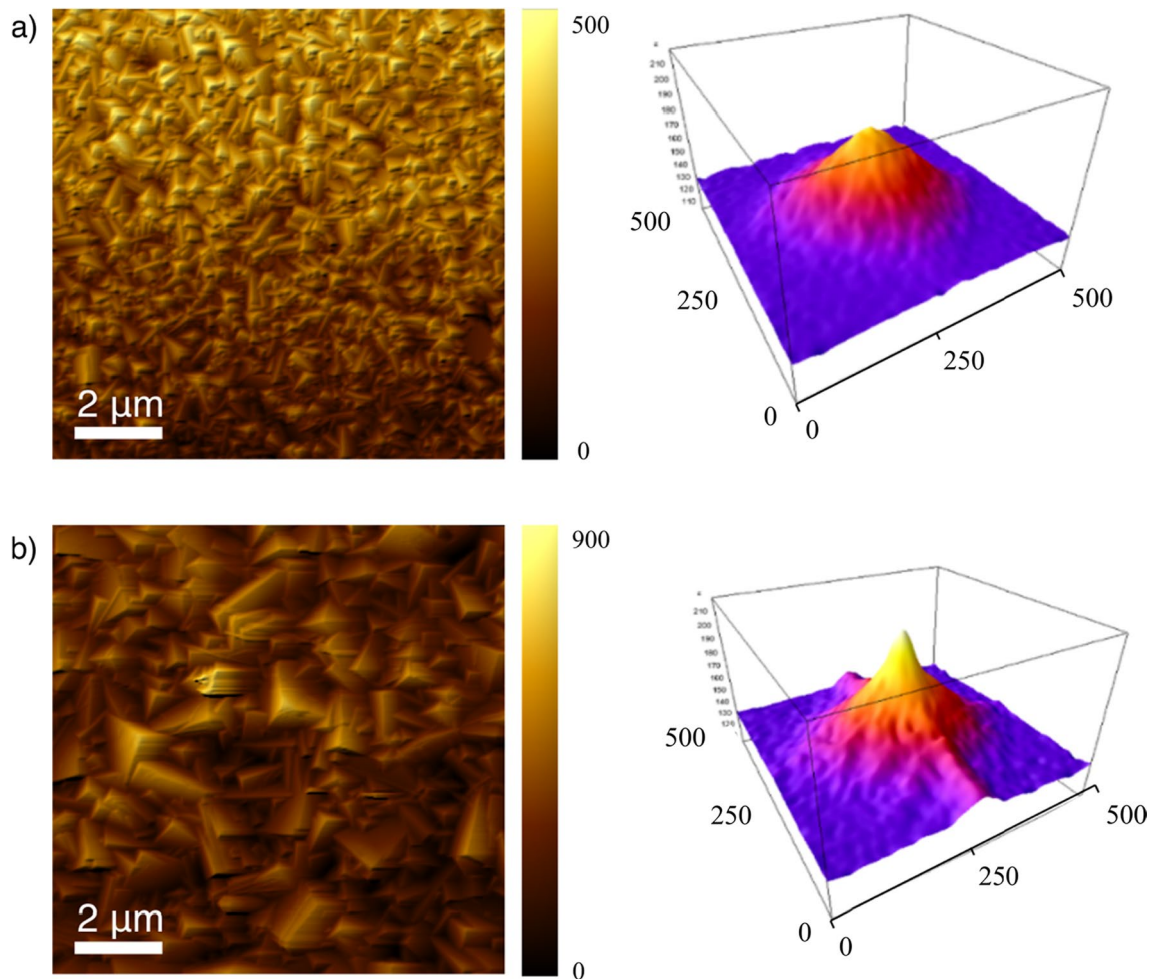**Fig. 1** Raman spectra of structures A and B

Fig. 2 AFM images and 2D FFT of **a)** sample A and **b)** sample B. Scanned area is 10×10 mm^2

Table 1 Results of the surface roughness analysis

	A	B
R_{RMS} (mm)	0.082	0.122
Ra (mm)	0.068	0.097
Rsk	0.001	0.409
Rku	−0.601	0.382

moment of the $h(x,y)$ distribution. The distribution of the $h(x,y)$ values is not symmetrical, the right tail of the distribution is slightly longer, and this effect is pronounced with the increasing forming temperature. The kurtosis value Rku is based on the fourth moment of the $h(x,y)$ distribution. It is significantly influenced by the outlier values. Compared to a normal distribution, sample distribution with a negative Rku has shorter and thinner tails and its central peak is lower and broader. The sample distribution with a positive Rku value has wider tails and a narrower shape of the distribution. These properties are well documented also by the shape of the histograms of the $h(x,y)$ function shown in Fig. 3. The $h(x,y)$ values are coded into 256 discrete values in the RGB color model. In the histograms of $h(x,y)$ values, the counts of individual values observed at the AFM image (counts axis) corresponding to 8 bit RGB model (value axis) are shown. The increasing forming temperature results in the production of structures with narrower distribution of surface shapes with higher peak value as documented in Fig. 2 and illustrated by narrower distribution of the height function in Fig. 3.

The properties of the formed microstructures were also analyzed by the fractal methods. The fractal geometry describes systems that are irregular at all scales of observation. The fractal analysis in our approach is based on the analysis of self-similarity and scaling properties of the $h(x,y)$ function values.[21, 22] We analyzed the multifractal singularity spectra $f(\alpha)$, generalized fractal dimension Dq and fractal succolarity σ. These functions are based on the statistical analysis of similarity and scaling properties of observed $h(x,y)$ values [23]. The plots of $f(\alpha)$ and Dq are shown in Fig. 4.
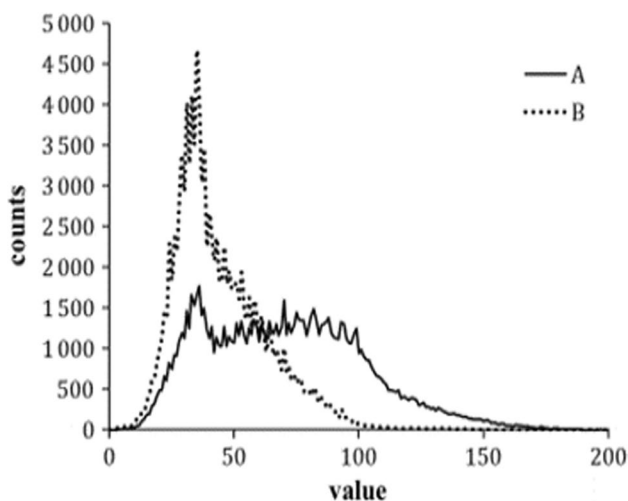
Fig. 3 Histograms of the $h(x,y)$ values determined from the AFM images of structures A and B

Multifractal functions $f(\alpha)$ and Dq show emphasized fractal features of the structure B and provide information about the microstructure properties with a high sensitivity to a applied technological operations. The humped shape of $f(\alpha)$ and the decreasing trend of Dq function are typical formultifractal structures and indicate that both structures A and B are non-Euclidean multifractals with complicated self-similar objects and different non-integer dimensions. A set of higher statistical moments q used in the analysis of the fractal scaling property was selected in interval -8 to 8. With the increased deposition temperature, the surface features show higher self-similarity and increased scaling property demonstrated by the higher variability of $f(\alpha)$ and Dq values shown in Fig. 4.

Fractal succolarity analysis is a new complementary approach in the multifractal analysis. Succolarity measures the percolation in the observed structure and enables to distinguish different types of surface textures that have similar fractal dimensions. The fractal dimension indicates how much the surface features occupy their underlying metric space. A succolarity of the fractal surface is defined as evaluation of the degree of filaments that allow percolation. The calculation of σ is based on box counting method implemented to the fractal succolarity algorithm [24, 25]. Binarized AFM images are examined in this approach using a series of boxes of defined sizes connected with the dividing factor. Succolarity is computed in four dimensions from left-to-right to top-to-bottom and finally average value σ_{AVG} is computed. The results of the fractal succolarity analysis are shown in Fig. 5a. The average fractal succolarity σ_{AVG} in a logarithmic dividing factor scale for given structure weakly depends on the dividing factor. On the other hand, σ_{AVG} values for sample B prepared at 50 °C is substantially lower. Increasing the deposition temperature decreases the number of bifurcations, which is important for the quality of the surface structure for the PEC applications.

The size distribution of particles observed at the AFM images was analysed in our approach using segmentation of the AFM images into a binary form. The resulting image was covered by boxes of different sizes followed by counting of the corresponding values in the given box area (intensity). The result of this analysis in log–log scale is shown in Fig. 5b. The variability of particle sizes rapidly decreases with the increasing deposition temperature to 50 °C as indicated by these results.

UV–Vis spectroscopy is suitable to analyze the properties of electronic structure of semiconducting and semi-insulating materials. We studied the properties of absorption coefficient a in $(\alpha h\nu)^z$ function dependence on photon energy $h\nu$, $(\alpha h\nu)^z = f(h\nu)$. The value of $z = 2$ is obviously used in study of allowed direct transitions in semiconductor structures. We computed energy band gap E_g of formed Cu_2O/FTO/ glass structure revealing the existence of such direct optical transitions. We constructed linear trend as tangent near point of maximal slope of the $(\alpha h\nu)^z$ function and estimated E_g by the determination of intersection of this linear trend with
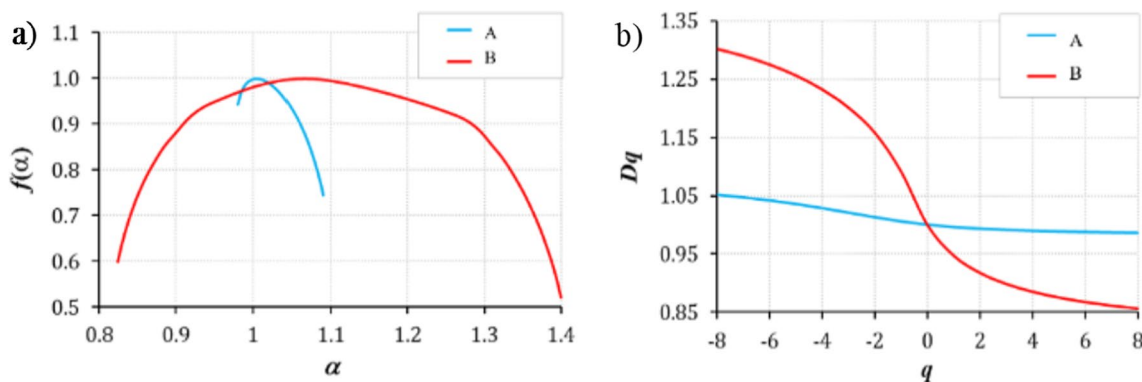

Fig. 4 **a**) Multifractal singularity spectrum $f(a)$; **b**) generalized fractal dimension Dq
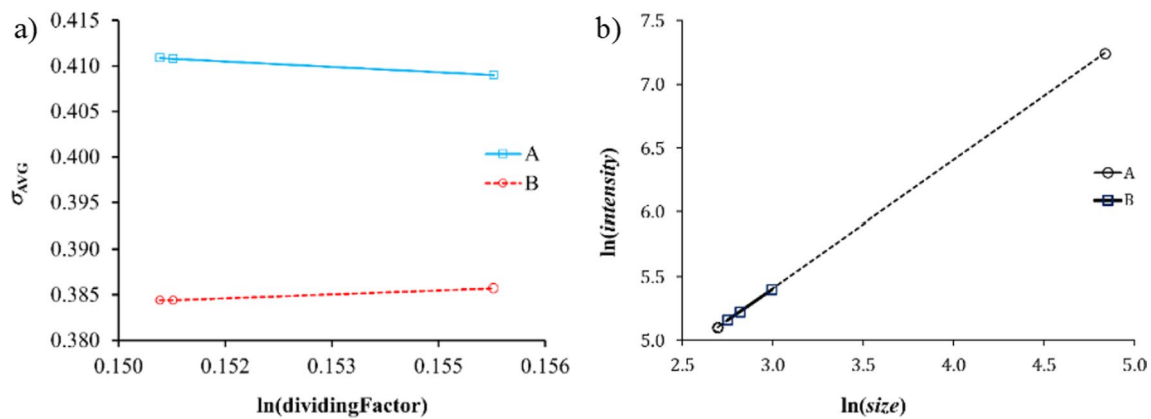
Fig. 5 Results of **a**) fractal succolarity and **b**) particle size analysis for structures A and B

the photon energy axis. Experimental values of the $(\alpha h \nu)^2$ function in the UV–Vis region and a regression of its linear part are shown in Fig. 6. Resulting values of energy gap are $E_g = 2.62 \pm 0.09$ eV for structure A and $E_g = 2.71 \pm 0.09$ eV for structure B, which are about 0.4 eV higher than the values reported in the literature [26].

4 Conclusion

In this work, we deposited cuprous oxide layers on the FTO/glass substrate and investigated the properties of structures formed under various temperature conditions. Microstructure properties were experimentally determined by the AFM and evaluated by statistical, fractal and Fourier methods. The results of optical absorption spectroscopy were used for the energy gap determination. Both structures, formed at 25 °C as well as 50 °C, were produced at relatively low temperatures without production of CuO phase. The forming temperature substantially modifies surface shape distributions. The roughness characteristics, 2D FFT, histograms and multifractal characteristics provide consistent information connected with the distribution of surface objects created during structure forming. Structures prepared at higher temperatures show higher variability of created surface objects, lower number of bifurcations and lower variability of particle sizes. By implementation of proposed methods, we obtained reliable information about the development of formed microstructure properties with the deposition temperature.
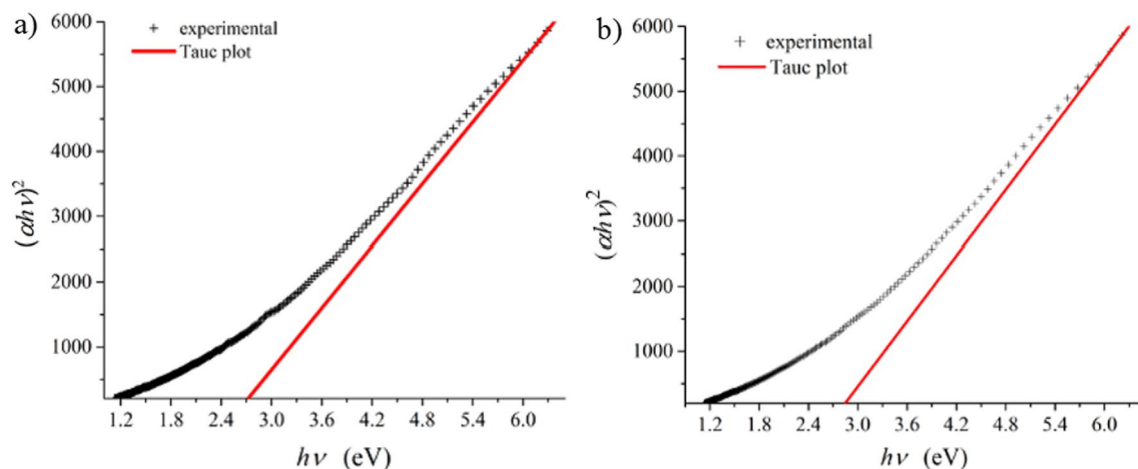

Fig. 6 Tauc method for the energy gap determination: **a**) structure A; **b**) structure B; experimental $(\alpha h \nu)^2$ function, line-linear regression of the Tauc plot

Declarations

References

1. G. Segev, J. Kibsgaard, C. Hahn, Z.J. Xu, W.-H. Cheng, T. Deutsch et al., The 2022 solar fuels roadmap. J Phys Appl Phys (2022). https://doi.org/10.1088/1361-6463/ac6f97
2. R. Wick, S.D. Tilley, Photovoltaic and photoelectrochemical solar energy conversion with Cu2O. J. Phys. Chem. C **119**, 26243–26257 (2015). https://doi.org/10.1021/acs.jpcc.5b08397
3. H. Zhang, Q. Zhu, Y. Zhang, Y. Wang, L. Zhao, B. Yu, One-pot synthesis and hierarchical assembly of hollow Cu2O microspheres with nanocrystals-composed porous multishell and their gas-sensing properties. Adv. Funct. Mater. **17**, 2766–2771 (2007). https://doi.org/10.1002/adfm.200601146
4. K.P. Musselman, A. Marin, L. Schmidt-Mende, J.L. MacManus-Driscoll, Incompatible length scales in nanostructured Cu2O solar cells. Adv. Funct. Mater. **22**, 2202–2208 (2012). https://doi.org/10.1002/adfm.201102263
5. R.P. Wijesundera, L.K.A.D.D.S. Gunawardhana, W. Siripala, Electrodeposited Cu2O homojunction solar cells: fabrication of a cell of high short circuit photocurrent. Sol Energy Mater Sol Cells. **157**, 881–6 (2016). https://doi.org/10.1016/j.solmat.2016.07.005
6. Y.A. Wu, I. McNulty, C. Liu, K.C. Lau, Q. Liu, A.P. Paulikas et al., Facet-dependent active sites of a single Cu2O particle photocatalyst for CO2 reduction to methanol. Nat. Energy **4**, 957–968 (2019). https://doi.org/10.1038/s41560-019-0490-3
7. L. Pan, J.H. Kim, M.T. Mayer, M.-K. Son, A. Ummadisingu, J.S. Lee et al., Boosting the performance of Cu 2 O photocathodes for unassisted solar water splitting devices. Nat. Catal. **1**, 412–420 (2018). https://doi.org/10.1038/s41929-018-0077-6
8. Q.-B. Ma, J.P. Hofmann, A. Litke, E.J.M. Hensen, Cu2O photoelectrodes for solar water splitting: tuning photoelectrochemical performance by controlled faceting. Sol. Energy Mater. Sol. Cells **141**, 178–186 (2015). https://doi.org/10.1016/j.solmat.2015.05.025
9. Z. Zhang, P. Wang, Highly stable copper oxide composite as an effective photocathode for water splitting via a facile electrochemical synthesis strategy. J. Mater. Chem. **22**, 2456–2464 (2012). https://doi.org/10.1039/C1JM14478B
10. A. Chen, H. Long, X. Li, Y. Li, G. Yang, P. Lu, Controlled growth and characteristics of single-phase Cu2O and CuO films by pulsed laser deposition. Vacuum **83**, 927–930 (2009). https://doi.org/10.1016/j.vacuum.2008.10.003
11. S. Jeong, E.S. Aydil, Heteroepitaxial growth of Cu2O thin film on ZnO by metal organic chemical vapor deposition. J. Cryst. Growth **311**, 4188–4192 (2009). https://doi.org/10.1016/j.jcrysgro.2009.07.020
12. Y. Yang, J. Han, X. Ning, W. Cao, W. Xu, L. Guo, Controllable morphology and conductivity of electrodeposited Cu2O thin film: effect of surfactants. ACS Appl. Mater. Interfaces **6**, 22534–22543 (2014). https://doi.org/10.1021/am506657v
13. X. Jiang, M. Zhang, S. Shi, G. He, X. Song, Z. Sun, Microstructure and optical properties of nanocrystalline Cu2O thin films prepared by electrodeposition. Nanoscale Res. Lett. **9**, 219 (2014). https://doi.org/10.1186/1556-276X-9-219
14. J. Morales, L. Sánchez, S. Bijani, L. Martínez, M. Gabás, J.R. Ramos-Barrado, Electrodeposition of Cu2O: an excellent method for obtaining films of controlled morphology and good performance in Li-ion batteries. Electrochem Solid-State Lett. **8**, A159 (2005). https://doi.org/10.1149/1.1854126
15. P. Wang, H. Wu, Y. Tang, R. Amal, Y.H. Ng, Electrodeposited Cu2O as photoelectrodes with controllable conductivity type for solar energy conversion. J. Phys. Chem. C **119**, 26275–26282 (2015). https://doi.org/10.1021/acs.jpcc.5b07276
16. S. Laidoudi, A.Y. Bioud, A. Azizi, G. Schmerber, J. Bartringer, S. Barre et al., Growth and characterization of electrodeposited Cu2O thin films. Semicond. Sci. Technol. **28**, 115005 (2013). https://doi.org/10.1088/0268-1242/28/11/115005
17. T.D. Golden, M.G. Shumsky, Y. Zhou, R.A. VanderWerf, R.A. Van Leeuwen, J.A. Switzer, Electrochemical deposition of copper(I) oxide films. Chem. Mater. **8**, 2499–2504 (1996). https://doi.org/10.1021/cm9602095
18. L.-C. Chen, C.-C. Chen, K.-C. Liang, S.H. Chang, Z.-L. Tseng, S.-C. Yeh et al., Nano-structured CuO-Cu2O complex thin film for application in CH3NH3PbI3 perovskite solar cells. Nanoscale Res. Lett. **11**, 402 (2016). https://doi.org/10.1186/s11671-016-1621-4
19. S. Jurečka, H. Angermann, H. Kobayashi, M. Takahashi, E. Pinčík, Multifractal analysis of textured silicon surfaces. Appl. Surf. Sci. **301**, 46–50 (2014). https://doi.org/10.1016/j.apsusc.2014.02.102
20. E. Magsipoc, Q. Zhao, G. Grasselli, 2D and 3D roughness characterization. Rock Mech. Rock Eng. **53**, 1495–1519 (2020). https://doi.org/10.1007/s00603-019-01977-4
21. S. Jurečka, H. Kobayashi, M. Takahashi, T. Matsumoto, M. Jurečková, F. Chovanec et al., On the influence of the surface roughness onto the ultrathin SiO2/Si structure properties. Appl. Surf. Sci. **256**, 5623–5628 (2010). https://doi.org/10.1016/j.apsusc.2010.03.030
22. A. Chhabra, R.V. Jensen, Direct determination of the f(\ensuremath{\alpha}) singularity spectrum. Phys. Rev. Lett. **62**, 1327–1330 (1989). https://doi.org/10.1103/PhysRevLett.62.1327
23. S. Jureckova, M. Jureckova, F. Chovanec, H. Kobayashi, M. Takahashi, M. Mikula et al., On the topographic and optical properties of SiC/SiO2 surfaces. Cent. Eur. J. Phys. **7**, 321–326 (2009). https://doi.org/10.2478/s11534-009-0021-0

24. R.H.C. de Melo, A. Conci, How Succolarity could be used as another fractal measure in image analysis. Telecommun. Syst. **52**, 1643–1655 (2013). https://doi.org/10.1007/s11235-011-9657-3

25. A. Block, W. von Bloh, H.J. Schellnhuber, Efficient box-counting determination of generalized fractal dimensions. Phys. Rev. A **42**, 1869–1874 (1990). https://doi.org/10.1103/PhysRevA.42.1869

26. I. Sullivan, B. Zoellner, P.A. Maggard, Copper(I)-based p-type oxides for photoelectrochemical and photovoltaic solar energy conversion. Chem. Mater. **28**, 5999–6016 (2016). https://doi.org/10.1021/acs.chemmater.6b00926